Key parameters for droplet evaporation and mixing at the cloud edge

Received: 19 October 2020 | Revised: 30 January 2021 | Accepted: 2 March 2021

DOI: 10.1002/qj.4015

Quarterly Journal of the Royal Meteorological Society RMetS

RESEARCH ARTICLE

Key parameters for droplet evaporation and mixing at the cloud edge

J. Fries[1] | **G. Sardina**[2] | **G. Svensson**[3] | **B. Mehlig**[1]

[1]Department of Physics, Gothenburg University, Gothenburg, Sweden

[2]Department of Mechanics and Maritime Sciences, Division of Fluid Dynamics, Chalmers University of Technology, Gothenburg, Sweden

[3]Department of Meteorology, Stockholm University and Swedish e-science Research Centre, Stockholm, Sweden

Correspondence
B. Mehlig, Department of Physics, Gothenburg University, SE-41296 Gothenburg, Sweden.
Email: bernhard.mehlig@physics.gu.se

Funding information
Vetenskapsrådet, Formas, Knut and Alice Wallenberg Foundation, Grant/Award Numbers: 2017-3865, 2014-585, 2014.0048

Abstract

The distribution of liquid water in ice-free clouds determines their radiative properties, a significant source of uncertainty in weather and climate models. Evaporation and turbulent mixing cause a cloud to display large variations in droplet number density, but quite small variations in droplet size (Beals *et al.*, Science, 2015, vol. 350, pp. 87–90). However, direct numerical simulations of the joint effect of evaporation and mixing near the cloud edge predict quite different behaviours, and how to reconcile these results with the experimental findings remains an open question. To infer the history of mixing and evaporation from observational snapshots of droplets in clouds is challenging, because clouds are transient systems. We formulated a statistical model that provides a reliable description of the evaporation–mixing process as seen in direct numerical simulations and allows us to infer important aspects of the history of observed droplet populations, highlighting the key mechanisms at work and explaining the differences between observations and simulations.

KEYWORDS

cloud microphysics, droplet evaporation, Lagrangian droplet dynamics, turbulent mixing

1 | INTRODUCTION

Clouds play a major role in regulating weather and climate on Earth, by modulating the incoming solar radiation. Despite substantial scientific advances in the last decades, clouds still represent the primary source of uncertainty in climate projections (Stocker *et al.*, 2013; Pincus *et al.*, 2018). A key challenge is to understand how entrainment of dry air at the edges of ice-free clouds affects the size distribution and number density of droplets (Blyth, 1993). This is important because the amount and distribution of liquid water determine cloud optical properties (Kokhanovsky, 2004) and precipitation efficiency (Burnet and Brenguier, 2007). As a consequence, weather and climate models are sensitive to how entrainment at the cloud edge is parameterised (Mauritsen *et al.*, 2012).

The optical properties of clouds are of crucial importance for the radiation balance of the Earth's climate system (Dufresne and Bony, 2008; Caldwell *et al.*, 2016). The size distribution and number density of droplets are key ingredients, because the light-extinction coefficient of the cloud is determined by the number of the droplets it contains times their average surface area (Kokhanovsky, 2004).

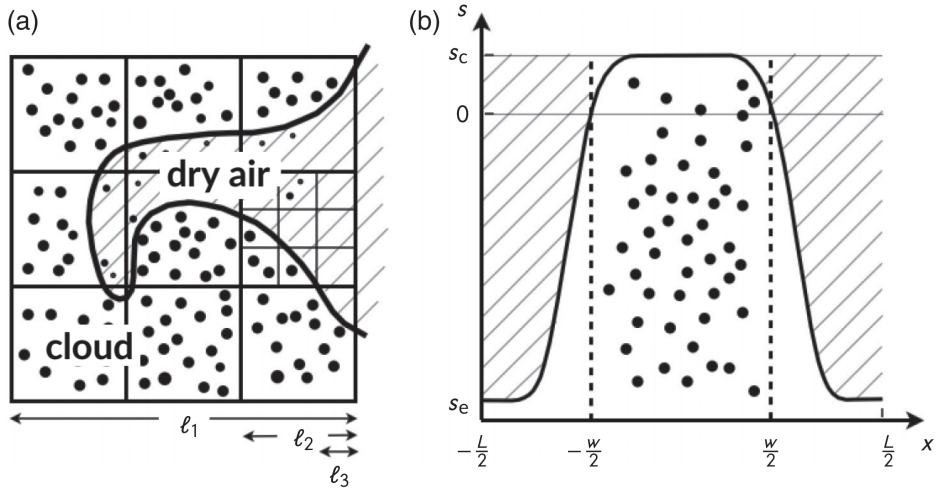

FIGURE 1 (a) Effect of mixing on local droplet populations (schematic). On large spatial scales (ℓ_1 and ℓ_2), mixing and evaporation is not yet complete, but some smaller regions (of size ℓ_3) are in local steady states: saturated air with droplets, or subsaturated air without droplets. (b) Initial cloud configuration in our model. Before mixing, moist air and droplets reside in a $w \times L \times L$ slab, contained in a cubic domain of side length L. Regions with dry air are dashed. The solid line is the initial profile of supersaturation s (see text).

Regarding precipitation efficiency, the mechanism of rain formation in ice-free clouds is a longstanding unresolved problem in atmospheric physics (Grabowski and Wang, 2013). A broad initial droplet size distribution is needed to activate the collisions and coalescences of droplets necessary for the rapid onset of rain formation observed empirically in warm clouds (Szumowski *et al.*, 1997; 1998; Devenish *et al.*, 2012). Microscopic droplets grow by condensation of water vapour, or shrink by evaporation. However, when a droplet-containing parcel does not mix with its surroundings, condensation causes the droplet size distribution to narrow because the diffusional growth of a droplet is inversely proportional to its radius, so that small droplets grow faster than large ones (Rogers and Yau, 1989).

Turbulence has a strong influence upon droplet condensation and evaporation in clouds (Bodenschatz *et al.*, 2010). Turbulent mixing causes water-vapour and liquid-water content to fluctuate on different length- and time-scales (Vaillancourt *et al.*, 2001). As a consequence, nearby droplets may have experienced quite different growth histories. The droplets of a cloudy parcel that is mixed with dry air evaporate at different rates, so that the droplet size distribution broadens (Lanotte *et al.*, 2009; Sardina *et al.*, 2015; 2018; Li *et al.*, 2020). Cloud-resolving simulations (Hoffmann and Feingold, 2019) show that this mechanism can have a strong effect on droplet number densities in turbulent clouds.

Entrainment of dry air at the cloud edge triggers rapid changes in the droplet size distribution (Perrin and Jonker, 2015; Abade *et al.*, 2018). As turbulence mixes dry air into the cloud, it creates long-lasting regions of dry air where droplets can evaporate rapidly. Droplets in regions with higher water-vapour concentration, by contrast, may saturate the air and survive for a much longer time (Figure 1a). While droplets evaporate, turbulence mixes the cloud at many length-scales, ranging from the Kolomogorov length—of the order of millimetres (Devenish *et al.*, 2012)—to a few kilometres (Rogers and Yau, 1989). Evaporation and mixing on a spatial scale ℓ depend on the turbulent mixing time τ_ℓ at that scale, and upon the relevant thermodynamic time-scale τ. Their ratio forms a Damköhler number $\mathrm{Da} = \tau_\ell/\tau$ (Dimotakis, 2005). The thermodynamic process parameterised by Da is limited by the rate of mixing if Da is large, and limited by thermodynamics if Da is small. The dynamics at large Damköhler numbers is referred to as inhomogeneous mixing (Baker *et al.*, 1980), where some droplets evaporate completely while others do not evaporate at all. Small-Da mixing is called homogeneous, where droplets evaporate at approximately the same rate, so that the droplet size distribution remains narrow.

The notion of homogeneous and inhomogeneous mixing remains debated (Tölle and Krueger, 2014), but it can be given a precise meaning in terms of the fraction $P_e(t)$ of droplets that have evaporated completely at time t. However, it is not understood at present which mechanisms and parameters determine the transition from homogeneous to inhomogeneous mixing. Several authors have attempted to describe turbulent mixing in terms of one Damköhler number. Lehmann *et al.* (2009) used a combined microphysical response time τ_r, a function of the two thermodynamic time-scales of the problem, τ_d (droplet evaporation), and τ_s (supersaturation relaxation). Lu *et al.* (2018), by contrast, suggest that τ_d should be used to formulate a single-parameter criterion for inhomogeneous mixing. The direct numerical simulations (DNS) by Kumar *et al.* (2018) explored how the nature of mixing changes as τ_L/τ_r increases with the linear size L of the simulated domain. However, no clear sign of inhomogeneous mixing was found. The authors mention that this may be a consequence of the thermodynamic setup used. Another possibility is that the simulated system was just not large enough. Jeffery (2007) emphasised that evaporation and

mixing cannot be described by a single Da alone, because there are two thermodynamic time-scales, leading to three key nondimensional parameters: $\mathrm{Da_d}$, $\mathrm{Da_s}$, and the volume fraction χ of cloudy air. However, Jeffery only studied the case $\mathrm{Da_d} = \mathrm{Da_s}$ and did not discuss the implications of varying the Damköhler numbers separately. Pinsky *et al.* (2016a) and Pinsky and Khain (2018a) modified an equation for advected liquid water (Rogers and Yau, 1989) into a diffusion–reaction equation for the droplet size distribution and emphasised the significance of a nondimensional parameter, their potential evaporation parameter.

Here we derive a statistical model for evaporation and turbulent mixing at the cloud edge from first principles. The model takes into account the multiscale turbulent dynamics, as turbulent clouds can have large Reynolds numbers; $\mathrm{Re} \sim 10^7$ is a conservative estimate for convective clouds (Devenish *et al.*, 2012). The model quantitatively predicts the outcomes of the DNS by Kumar *et al.* (2012; 2013; 2014; 2018). Furthermore, the model shows, in accordance with Jeffery (2007), that the evolution of the droplet size distribution is determined by $\mathrm{Da_d}$, $\mathrm{Da_s}$, and χ. We find that the potential evaporation parameter of Pinsky *et al.* (2016a) and Pinsky and Khain (2018a) is determined simply by the ratio of the Damköhler numbers. Finally, the model allows us to interpret the results of in situ measurements of clouds at the centimetre scale (Beals *et al.*, 2015).

2 | METHOD

We study mixing and evaporation of cloud droplets by mixing moist air, droplets, and dry air in a cubic domain of side length L with periodic boundary conditions. Initially, the saturated or slightly supersaturated moist air with supersaturation $s_\mathrm{c} \geq 0$ is contained in a $w \times L \times L$ slab, together with N_0 randomly distributed water droplets (Figure 1b). The dry air, initially outside the slab, has negative supersaturation $s_\mathrm{e} < 0$. The mixing is driven by statistically stationary homogeneous isotropic turbulence, with turbulent kinetic energy TKE and mean dissipation rate per unit mass ϵ (Frisch, 1995). Essentially the same setup is used in the DNS of Kumar *et al.* (2012; 2013; 2014; 2018), which allows us to understand their simulation results in terms of our model.

2.1 | Microscopic equations

For the turbulent mixing, we start from the microscopic equations of Kumar *et al.* (2018) and earlier studies (Vaillancourt *et al.*, 2002; Lanotte *et al.*, 2009; Paoli and Shariff, 2009; Kumar *et al.*, 2014; Perrin and Jonker, 2015). We neglect buoyancy, particle inertia and settling, temperature changes due to vertical motion, and temperature and pressure dependences of the thermodynamic coefficients, and subsume the joint effects of temperature and water vapour into a single supersaturation field.

We denote fluid velocity and pressure by $\boldsymbol{u}(\boldsymbol{x}, t)$ and $p(\boldsymbol{x}, t)$, and supersaturation by $s(\boldsymbol{x}, t)$. The spatial position of droplet α is $\boldsymbol{x}_\alpha(t)$, its radius equals $r_\alpha(t)$, and the index α ranges from 1 to N_0. We nondimensionalise as follows: $\boldsymbol{u}' = \boldsymbol{u}/U$, $\boldsymbol{x}' = \boldsymbol{x}/(U\tau_L)$, $t' = t/\tau_L$, $p' = p/(\varrho_\mathrm{a} U^2)$, $\boldsymbol{x}'_\alpha = \boldsymbol{x}_\alpha/(U\tau_L)$, $s' = s/|s_\mathrm{e}|$, $r'_\alpha = r_\alpha/r_0$, and $s'_\mathrm{c} = s_\mathrm{c}/|s_\mathrm{e}|$. Here $U = \sqrt{2\,\mathrm{TKE}/3}$ is the turbulent root-mean-square velocity, $\tau_L = \mathrm{TKE}/\epsilon$ is the large-eddy time [proportional to L/U if the size of the largest eddies is of the order L (Pope, 2000)], ϱ_a is the reference mass density of air, $r_0 = [N_0^{-1} \sum_{\alpha=1}^{N_0} r_\alpha(0)^3\,]^{1/3}$ is the initial volume-averaged droplet radius, and $|s_\mathrm{e}|$ is the (positive) subsaturation of air outside the initial cloud slab. Dropping the primes, the microscopic equations take the nondimensional form:

$$\frac{D}{Dt}\boldsymbol{u} = -\nabla p + \mathrm{Re}_L^{-1}\nabla^2\boldsymbol{u} \quad \text{with} \quad \nabla\cdot\boldsymbol{u} = 0, \tag{1}$$

$$\frac{D}{Dt}s = (\mathrm{Re}_L\mathrm{Sc})^{-1}\nabla^2 s - \mathrm{Da_s}\;\chi V\overline{r_\alpha(t)s(\boldsymbol{x}_\alpha, t)}, \tag{2}$$

$$\frac{d}{dt}\boldsymbol{x}_\alpha = \boldsymbol{u}(\boldsymbol{x}_\alpha, t)\;, \tag{3}$$

$$\frac{d}{dt}r_\alpha = \mathrm{Da_d}\;s(\boldsymbol{x}_\alpha(t), t)/(2r_\alpha) \quad \text{if } r_\alpha > 0\;. \tag{4}$$

Equations 1–4 are the incompressible Navier–Stokes equations, with Lagrangian time derivative $\frac{D}{Dt} = \partial_t + (\boldsymbol{u}\cdot\nabla)$. In DNS of Equations 1–4, a forcing is imposed to sustain stationary turbulence. This is not necessary in the model introduced below, and we therefore do not include a forcing term in Equation 1. Equation 2 is the equation for supersaturation. The first term on its right-hand side describes diffusion of the supersaturation $s(\boldsymbol{x}, t)$. The second term models the effect of condensation and evaporation through the average $\overline{r_\alpha(t)s(\boldsymbol{x}_\alpha, t)}$, taken over all droplets in the vicinity of $\boldsymbol{x}$. Droplets are advected by the turbulent flow (Equation 3), and Equation 4 models how the droplet radius r_α changes due to evaporation and condensation. When a droplet has evaporated completely, we impose that it must remain at $r_\alpha = 0$. In the derivation of Equation 4, $s(\boldsymbol{x}_\alpha(t), t)$ enters as the supersaturation at distances from the droplet much larger than the droplet radius (Rogers and Yau, 1989). In other words, Equation 4 relies on a scale separation between droplet sizes and the lengths that characterise supersaturation fluctuations generated by turbulent mixing (Vaillancourt *et al.*, 2001). As

a consequence, droplets interact locally with the supersaturation field over finite volumes through the average $\overline{r_\alpha(t)s(\boldsymbol{x}_\alpha,t)}$ in Equation 2. Further details regarding Equations 1–4 are given in the Supporting Information, where we also show how to derive Equations 1–4 from the more detailed dynamical description of Vaillancourt *et al.* (2001; 2002), Kumar *et al.* (2014; 2018), and Perrin and Jonker (2015).

An advantage of writing the dynamics in nondimensional form is that this determines the independent nondimensional parameters. First, $\mathrm{Re}_L = \frac{2}{3}\mathrm{TKE}^2/(\varepsilon\nu)$ is the turbulence Reynolds number (Pope, 2000), where ν is the kinematic viscosity of air. The Schmidt number is defined as $\mathrm{Sc} = \nu/\kappa$, where κ is the diffusivity of s. The volume fraction of cloudy air is given by $\chi = w/L$, and $V = [L/(U\tau_L)]^3$ is the dimensionless domain volume. The Damköhler number $\mathrm{Da_s}$ is defined as $\mathrm{Da_s} = \tau_L/\tau_\mathrm{s}$, where $\tau_\mathrm{s} = (4\pi A_2 A_3 \varrho_\mathrm{w} n_0 r_0)^{-1}$ is the supersaturation relaxation time. This is the time-scale at which the supersaturation decays towards saturation, assuming that all droplets have the same radius r_0, and for droplet number density $n_0 = N_0/(wL^2)$. Further, ϱ_w is the density of pure liquid water, and A_2 and A_3 are thermodynamic coefficients, specified in the Supporting Information. The Damköhler number $\mathrm{Da_d}$ is defined as $\mathrm{Da_d} = \tau_L/\tau_\mathrm{d}$, where $\tau_\mathrm{d} = r_0^2/(2A_3|s_\mathrm{e}|)$ is the droplet evaporation time, the time that it takes for a droplet of radius r_0 to evaporate completely in a constant ambient supersaturation $s_\mathrm{e} < 0$.

The Damköhler numbers determine the extent to which saturation and droplet evaporation are limited by the rate of mixing (Dimotakis, 2005). Saturation is mixing-limited at large $\mathrm{Da_s}$, since regions with evaporating droplets—created by mixing of cloudy and dry air at the time-scale τ_L—saturate faster than τ_L. When $\mathrm{Da_s}$ is small, by contrast, evaporating droplets saturate the air more slowly than it is mixed. In this case, saturation is not limited by the rate of mixing. Droplet evaporation is mixing-limited at large $\mathrm{Da_d}$, since droplets then evaporate more rapidly than the exposure to subsaturated air changes. At small $\mathrm{Da_d}$, mixing is faster than droplet evaporation, and droplets tend to evaporate mainly after the system has been mixed. The droplets then experience roughly the same supersaturation as they evaporate.

In the limit $\mathrm{Re}_L \to \infty$, three key nondimensional parameters remain in Equations 1–4: χ, $\mathrm{Da_d}$, and $\mathrm{Da_s}$. The system can be parameterised by χ, $\mathrm{Da_d}$, and

$$\mathscr{R} = \mathrm{Da_d}/\mathrm{Da_s}\,. \tag{5}$$

In this way, the scale dependence of the mixing process is contained in $\mathrm{Da_d}$ only. The Damköhler-number ratio $\mathscr{R}$ is inversely proportional to the density of liquid water in the cloud slab; it regulates the moisture of the mixing process (details in the Supporting Information). The bifurcation between moist steady states, where droplets remain in saturated air, and dry steady states, where all droplets have evaporated completely (Jeffery, 2007; Kumar *et al.*, 2013; Pinsky *et al.*, 2016b), occurs at a critical value of $\mathscr{R}$, $\mathscr{R}_\mathrm{c}$. The critical ratio $\mathscr{R}_\mathrm{c}$ can be computed from the conserved quantity $\theta = -\langle s(t)\rangle - \frac{2\chi}{3\mathscr{R}}[1 - P_\mathrm{e}(t)]\langle r^3(t)\rangle$, which is analogous to the liquid-water potential temperature at fixed altitude (Gerber *et al.*, 2008; Lamb and Verlinde, 2011; Kumar *et al.*, 2014). Here, $P_\mathrm{e}(t)$ is the fraction of completely evaporated droplets, the fraction of droplets for which $r_\alpha(t) = 0$ at time t. Furthermore, $\langle s(t)\rangle = V^{-1}\int_V s(\boldsymbol{x},t)\,d\boldsymbol{x}$ is the volume average of supersaturation, and $\left\langle r^3(t)\right\rangle = \{[1 - P_\mathrm{e}(t)]N_0\}^{-1}\sum_{\alpha=1}^{N_0} r_\alpha(t)^3$ is the mean cubed droplet radius, conditioned on $r_\alpha(t) > 0$ by the factor $[1 - P_\mathrm{e}(t)]^{-1}$. The conservation of θ can be concluded by integrating Equation 2 for supersaturation over the domain volume: see the Supporting Information for details. Moist steady states have $\left\langle r^3(t)\right\rangle > 0$ and $\langle s(t)\rangle = 0$, dry steady states have $P_\mathrm{e}(t) = 1$ and $\langle s(t)\rangle < 0$, so the sign of θ determines whether the steady state is moist or dry. The value of θ is determined by the initial conditions, $\theta = -\langle s(0)\rangle - 2\chi/(3\mathscr{R})$. Setting $\theta = 0$, we find the critical Damköhler-number ratio $\mathscr{R}_\mathrm{c} = -\frac{2}{3}\chi/\langle s(0)\rangle$.

DNS of Equations 1–4 for experimentally observed dissipation rates and droplet number densities are feasible only for quite small systems (Kumar *et al.*, 2018). This restricts the range of scales that can be explored and makes it difficult to detect inhomogeneous mixing in DNS. We therefore pursue an alternative approach and adapt a PDF model (Pope, 2000)—commonly used to describe combustion processes (Haworth, 2010)—to the inhomogeneous cloud edge. As opposed to the kinematic statistical models reviewed by Gustavsson and Mehlig (2016), we must also take thermodynamic processes into account.

2.2 | Statistical model

Statistical models have been used to describe droplets in a supersaturation field that fluctuates around zero, as in the cloud core (Paoli and Shariff, 2009; Sardina *et al.*, 2015; Chandrakar *et al.*, 2016; Siewert *et al.*, 2017). At the cloud edge, there are large deviations from this equilibrium. Jeffery (2007), Pinsky *et al.* (2016a), and Pinsky and Khain (2018a) formulated models for the cloud edge where droplets evaporate in direct response to a mean supersaturation field. This does not take into account that mixing is local, and that small droplets are advected together with the supersaturation field. For an accurate description of mixing and evaporation, it is essential to describe how each

droplet carries its own local supersaturation (Siewert *et al.*, 2017). Our model does just that. It is derived from first principles using the established framework of PDF models (Pope, 2000).

For the configuration shown in Figure 1b, we derive one-dimensional statistical-model equations from Equations 1–4 (details in the Supporting Information):

$$du = -\frac{3}{4}C_0 u dt + \left(\frac{3}{2}C_0\right)^{1/2} d\eta \ , \tag{6}$$

$$\frac{d}{dt}s = -\frac{1}{2}C_\phi[s - \langle s(x,t)\rangle] - \mathrm{Da_s}\ \chi V \langle r(t)s(x,t)\rangle \ , \tag{7}$$

$$\frac{d}{dt}x = u \ , \tag{8}$$

$$\frac{d}{dt}r = \mathrm{Da_d}\ s/(2r) \quad \text{if} \quad r > 0 \ . \tag{9}$$

Equation 6 describes the fluctuating acceleration of Lagrangian fluid elements in turbulence. Here, $d\eta$ are Brownian increments with zero mean and variance dt, and C_0 is an empirical constant (Pope, 2011). Each Lagrangian fluid element has a supersaturation s, and may contain a droplet (at position x, of size r). Equation 7 approximates the supersaturation dynamics as decay towards $\langle s(x,t)\rangle$, regulated by the empirical constant C_ϕ (Pope, 2000). The second term on the right-hand side of Equation 7 represents the effect of condensation and evaporation through $\langle r(t)s(x,t)\rangle$. The position-dependent averages $\langle \dots \rangle$ in Equation 7 are taken over fluid elements located at x at time t (details in the Supporting Information). The statistical model in Equations 6–9 becomes independent of Re_L at large Reynolds numbers, where C_0 approaches a definite limit (Pope, 2011). It is independent of Sc, in accordance with the known behaviour of advected scalars in fully developed turbulence (Shraiman and Siggia, 2000).

Equations 6–9 rest upon a probabilistic description of the dynamics of the two phases, droplets and air (Pope, 2000; Jenny *et al.*, 2012). The corresponding evolution equations, dictated by Equations 1–4, contain unclosed terms that must be approximated (Pope, 1985; Haworth, 2010) to obtain a closed model such as in Equations 6–9. Following Pope (2000), we cast the model into the form of stochastic dynamical equations for Lagrangian fluid elements. Since the dynamics is statistically one-dimensional in our configuration, we can average over the y and z coordinates to obtain Equations 6–9 in one-dimensional form. For the closures, we rely on standard approximations, common and justified in PDF modelling of single-phase flows (Pope, 1985) and in models for turbulent combustion (Haworth, 2010; Jenny *et al.*, 2012; Stöllinger *et al.*, 2013). The explicit mathematical approximations for the closures provided in the Supporting Information render the interpretation of the statistical model definite, and indicate how to improve the model when necessary.

In the following, we briefly summarise the closures. Equation 6 contains the closure for fluid-element accelerations. It reproduces the empirically observed effect of turbulent diffusion of passive-scalar averages (Pope, 2000). Equation 7 contains two closure approximations. First, the decay towards $\langle s(x,t)\rangle$ approximates the diffusion of supersaturation. This closure ensures that the mean of a passive scalar is conserved, and that a passive scalar remains bounded between its minimal and maximal values (Pope, 2000). Furthermore, it describes the decay of passive-scalar variance in statistically homogeneous turbulent mixing of two scalar concentrations (Pope, 2000). However, this closure does not reproduce the relaxation of the single-point PDF of scalar concentration from a two-peaked distribution via a U-shaped distribution into a Gaussian (Eswaran and Pope, 1988; Pope, 1991). For our initial conditions (Figure 1b), the decay towards $\langle s(x,t)\rangle$ captures the supersaturation fluctuations experienced by a fluid element as it moves towards or away from the most cloudy region. Note that this closure does not account for large saturated cloud structures that tend to relax slowly towards $\langle s(x,t)\rangle$. Such events are most relevant during the initial stages of the mixing–evaporation process, and their effect is expected to diminish with time, as large cloud structures are mixed into smaller and smaller structures. Consequently, the statistical model may describe short initial transients only qualitatively, not quantitatively.

The second closure in Equation 7 approximates the effects of droplet phase change on the supersaturation field: the local average $\overline{r_\alpha(t)s(\boldsymbol{x}_\alpha,t)}$ in Equation 2 is replaced by the ensemble average $\langle r(t)s(x,t)\rangle$. This is the simplest closure that preserves the conservation of the parameter θ, and it is therefore common in PDF models that describe combustion of particles in turbulence (Haworth, 2010; Jenny *et al.*, 2012; Stöllinger *et al.*, 2013). The average $\langle r(t)s(x,t)\rangle$ takes into account that droplet evaporation is delayed locally when nearby droplets saturate the surrounding air. Since we obtain closure by replacing the local average $\overline{r_\alpha(t)s(\boldsymbol{x}_\alpha,t)}$ by an average over fluid elements with one-dimensional dynamics, variations in the rate of supersaturation relaxation in the y- and z-coordinates are not described.

It is expected that the large cloud structures mentioned above, and their three-dimensional forms, matter more at very large Damköhler numbers. Therefore it cannot be excluded that the statistical model is only qualitative in this extreme limit. Below we show that the model works very well even for the largest Damköhler numbers in DNS studies (Kumar *et al.*, 2012; 2014). Also, since the statistical model is derived using the established framework of PDF models (Pope, 2000), it can be improved straightforwardly

by incorporating additional variables in the probabilistic description (Pope and Chen, 1990; Pope, 2000; Meyer and Jenny, 2008), or by using more refined approximations (Pope, 1991; Jenny *et al.*, 2012).

3 | RESULTS

3.1 | Comparison with DNS

The statistical model can be used to understand the DNS results of Kumar *et al.* (2012; 2013; 2014; 2018). Figure 2 shows good agreement for the time evolution of the fraction $P_e(t)$ of droplets that have completely evaporated, even though the statistical-model dynamics is slightly slower. Panels (a) and (b) in Figure 3 shows that the model reproduces the broadening of the droplet size distribution. The slightly slower dynamics in Figure 2 and the deviations in the tails in Figure 3 suggest that the statistical model does not reproduce the most rapid evaporation rates. This could be due to turbulent fluctuations in the supersaturation diffusion, neglected in Equation 7. Kumar *et al.* (2012; 2014) compute droplet size distributions with prominent exponential tails using DNS—some of them are seen in Figure 3 (black lines)—and connect these tails to corresponding exponential tails in the PDF of supersaturation at droplet positions. In our statistical-model simulations, we observe heavy tails in the PDF of supersaturation at droplet positions, but the tails are less pronounced than in the DNS (not shown). Heavy tails are consistent with the results of Eswaran and Pope (1988) mentioned above, who observed how an initially bimodal supersaturation relaxes.

Despite these shortcomings, our model describes the time evolution of $P_e(t)$ very well (Figure 2). It is also a significant improvement over models in which the droplets interact with a mean supersaturation field (Jeffery, 2007; Pinsky *et al.*, 2016a; Pinsky and Khain, 2018a). In reality, the droplets react to the local supersaturation, as mentioned above, and this may be particularly important at large values of $\mathrm{Da_d}$, where locally saturated regions can persist for a long time.

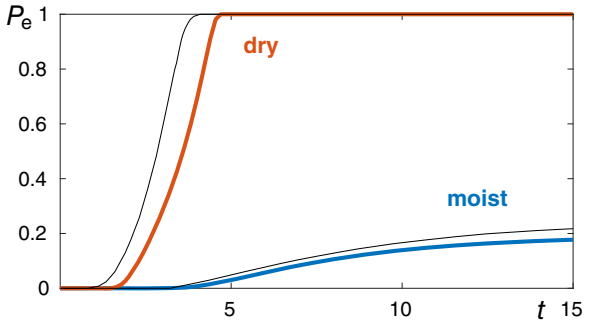

FIGURE 2 Fraction $P_e(t)$ of droplets that have evaporated completely as a function of nondimensional time t, parameters in Table 1. Coloured lines are statistical-model simulations, black lines are DNS of Kumar *et al.* (2014).

Figure 4 shows the steady-state value P_e^* of $P_e(t)$ computed from the statistical model as a function of $\mathrm{Da_d}$ and $\mathscr{R}/\mathscr{R}_c$. We see how P_e^* increases with both $\mathrm{Da_d}$ and $\mathscr{R}/\mathscr{R}_c$. The DNS results of Andrejczuk *et al.* (2006) and Kumar *et al.* (2012; 2013; 2014; 2018) form a pattern in Figure 4 that verifies these dependences: open symbols correspond to DNS with little or no complete evaporation in the steady state ($P_e^* < 10\%$), and filled symbols to $P_e^* > 10\%$. Figure 4 also explains why the DNS of Kumar *et al.* (2018) did not exhibit significant levels of inhomogeneous mixing: since their $\mathscr{R}$ was quite small, small values of P_e^* require values of $\mathrm{Da_d}$ much larger than unity ($\mathrm{Da_d} \sim 10^2$ for $P_e^* = 10\%$). Furthermore, the substantially different outcomes of the DNS of Kumar *et al.* (2012; 2014) are explained: their parameters lie on opposite sides of the bifurcation line. Figure 4 also explains, at least qualitatively, numerical results of DNS of transient turbulence with quite different initial conditions (Andrejczuk *et al.*, 2006), namely how the amount of complete droplet evaporation increases with both $\mathscr{R}/\mathscr{R}_c$ and $\mathrm{Da_d}$. There is no parameter corresponding directly to $\mathrm{Da_d}$ in the simulations of Andrejczuk *et al.* (2006), because they are for different initial conditions and flows. We therefore place these simulations in Figure 4 by computing a time-scale ratio that, in a qualitative sense, incorporates the same physics as $\mathrm{Da_d}$ (details in the Supporting Information). Key parameters of the DNS in Figure 4 are summarised in Table 2; a complete description is provided in the Supporting Information.

3.2 | Mixing histories from observations

A common way of characterising the droplet content of a cloud is to plot the mean cubed radius r^3 and number density n of droplets for observed cloud-droplet populations in a mixing diagram. Figure 5(a) shows a mixing diagram with empirical data from Beals *et al.* (2015). Black crosses are values of r^3 and n extracted from snapshots (linear size 15 cm) of local droplet populations measured during an airplane flight through a convective cloud.

Observational data in mixing diagrams are commonly discussed in relation to the homogeneous mixing line, a curve of the global steady states (r_*^3, n_*) that result from homogeneous mixing (no complete evaporation) between different proportions of undiluted cloudy and dry environmental air (Gerber *et al.*, 2008; Kumar *et al.*, 2014; Pinsky *et al.*, 2016a). Beals *et al.* (2015) calculated this line; it is also

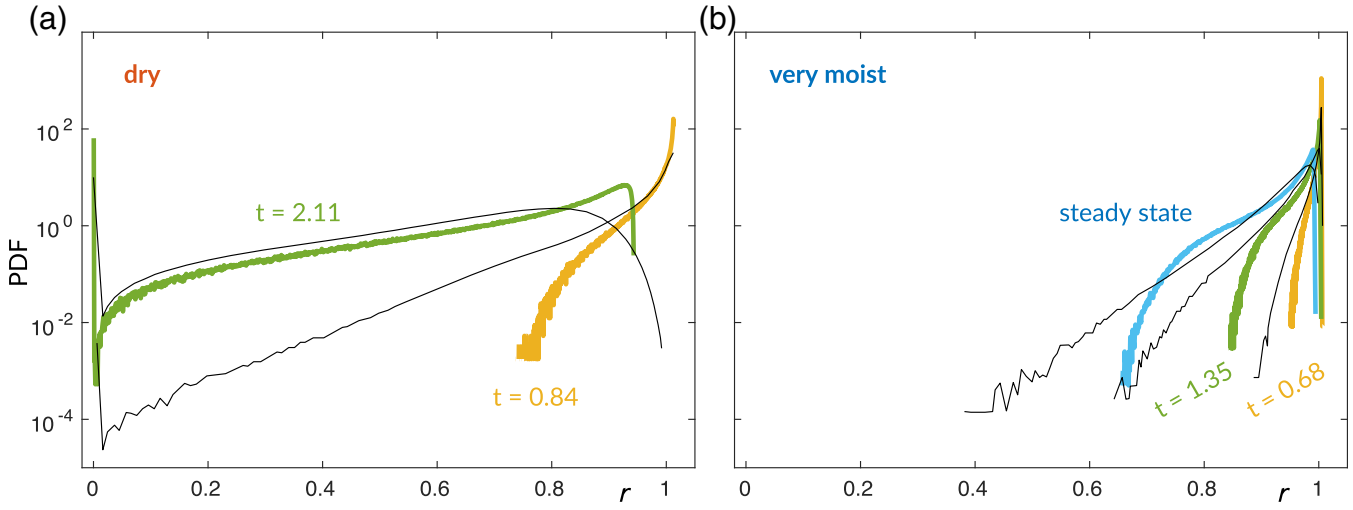

FIGURE 3 (a) Evolution of the droplet size distribution (parameters in Table 1) for different times. The probability density of the nondimensional droplet radius r is shown for the statistical model (coloured lines) and DNS of Kumar *et al.* (2014) (black lines). The initial droplet size distribution is monodisperse and centred at $r = 1$. (c) Same as (b), but for a very moist case (parameters in Table 1) and DNS of Kumar *et al.* (2012).

TABLE 1 Summary of statistical-model simulations (details in the Supporting Information): Damköhler number ratio $\mathscr{R}$, critical ratio $\mathscr{R}_c$, and volume fraction χ of cloudy air.

Simulation	Da_d	Da_s	$\mathscr{R}$	$\mathscr{R}_c$	χ
Figure 2 and 3a [dry]	2.44	0.968	2.52	0.859	0.428
Figure 2 [moist]	1.09	1.43	0.76	0.859	0.428
Figure 3b [very moist]	0.754	8.20	0.092	0.683	0.4
Figure 4	5E-3–4E2	1E-3–9E3	4E-2–4E0	0.913	0.429
Figure 5a	1E-2–1E3	6E-2–6E3	0.17	0.18–2.7	0.2–0.8
Figure 5b	1E-2–8E2	3E-3–4E4	2.4E-2–2.9E-2	0.38–0.41	0.369–0.374

shown in Figure 5a. A fundamental problem, however, is that it is not clear how to interpret mixing diagrams such as Figure 5a, since it is not clear that the empirically observed droplet populations reflect global steady states (Pinsky and Khain, 2018a).

It is nevertheless likely that most data points in Figure 5a sample local steady states, that is, locally well-mixed droplet populations that reside in saturated air. To describe such droplet populations, one must refer to the multiscale turbulent mixing process. We attempted this analysis using the statistical model, assuming that the statistical model with the initial condition shown Figure 1b describes how a cloud structure at the spatial scale L develops. Under this assumption, n_* and r_*^3 are given by the droplet number density (normalised by n_0) and the mean cubed droplet radius $\langle r(t)^3 \rangle$ in the steady state, and we can conjecture the mixing histories that formed the measured droplet populations.

We begin by noting that χ and P_e^* are completely determined for any steady-state point (r_*^3, n_*) in a mixing diagram. To show this, we write the volume-averaged initial supersaturation as $\langle s(0) \rangle = (1 + s_c)(\chi + \chi_0) - 1$, where χ_0 is a constant that depends on the initial supersaturation profile (details in the Supporting Information). Inserting

$$\chi = n_*/(1 - P_e^*) \tag{10}$$

into $\theta = -\langle s(t) \rangle - \frac{2\chi}{3\mathscr{R}}[1 - P_e(t)]\langle r^3(t) \rangle$, we find

$$P_e^* = 1 - \frac{n_*[1 + \frac{3}{2}\mathscr{R}(1 + s_c)]}{n_* r_*^3 + \frac{3}{2}\mathscr{R}[1 - \chi_0(1 + s_c)]} . \tag{11}$$

Equations 10 and 11 determine how to map (r_*^3, n_*) to (χ, P_e^*). As a consistency check we note that one obtains the homogeneous mixing line (Pinsky *et al.*, 2016a) from Equation 11 by setting $P_e^* = 0$. This allows us to infer that

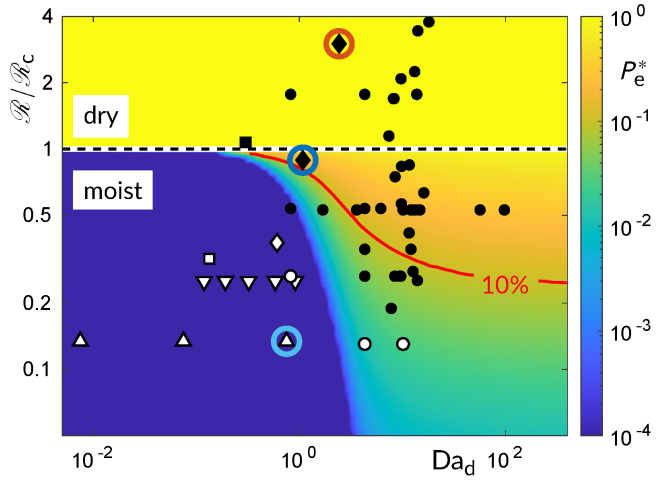

FIGURE 4 Steady-state fraction P_e^* of completely evaporated droplets as a function of Da_d and $\mathscr{R}/\mathscr{R}_c$; details in the Supporting Information. The fraction P_e^* is colour-coded. The solid red line is the contour $P_e^* = 10\%$, the black dashed line indicates the transition between moist and dry steady states, and symbols indicate DNS results from previous studies: △ (Kumar *et al.*, 2012), □ (Kumar *et al.*, 2013), ◇ (Kumar *et al.*, 2014), ▽ (Kumar *et al.*, 2018), and ○ (Andrejczuk *et al.*, 2006). Filled symbols indicate $P_e^* > 10\%$. The DNS of Andrejczuk *et al.*, (2006) should not be compared quantitatively with the statistical model results, since they are for different initial conditions and decaying turbulence (see text and Supporting Information). Red, blue, and light blue circles correspond to the dry, moist, and very moist simulations in Figures 2 and 3.

$\mathscr{R} = 0.17$ and $s_c = \chi_0 = 0$ for the homogeneous mixing line of Beals *et al.* (2015).

Any point in the mixing diagram must correspond to a local steady state with certain values of P_e^* and χ. Each statistical-model simulation for given Da_d, $\mathscr{R}$, and χ yields a certain value of P_e^*. This allows us to extract a value of Da_d for each point in the mixing diagram from our statistical-model simulations. The result is shown in Figure 5a. We see that Da_d increases rapidly above the homogeneous mixing line. Estimating $\tau_s \sim 1$s from Beals *et al.* (2015) and conservatively estimating $\varepsilon \sim 1$ cm^2·s^{-3} for a convective cloud, a value of $Da_d = 1000$ implies that an observed droplet population was mixed at spatial scales of the order of $L \sim \sqrt{\varepsilon \tau_L^3} \sim$ 5 km, larger than the size of the cloud. In other words, the rapid increase of Da_d in Figure 5a suggests that most of the data in the mixing diagram cannot be in a global steady state of a mixing process parameterised by $\mathscr{R} = 0.17$.

We concluded above that most measurements of Beals *et al.* (2015) are likely to correspond to local steady states. As undiluted cloudy air is mixed with premixed air, such steady states are formed locally and temporarily as local mixing processes equilibrate at small spatial scales (Figure 1a). We now discuss how the analysis of local steady states may yield insight into possible local histories of the cloud. Air affected by earlier mixing events is not as dry as environmental air, so the mixing of undiluted cloud with premixed air is governed by smaller values of $\mathscr{R}$. We therefore ask: which values of $\mathscr{R}$ are consistent with the assumption that the experimentally observed droplet population in the middle panel of figure 2 of Beals *et al.* (2015)—the red cross in Figure 5a—reflects a local steady state? Our model allows us to determine possible combinations of Da_d, $\mathscr{R}$, and χ consistent with a local steady state. We know that $\mathscr{R}$ must be smaller than 0.17, the upper limit dictated by the homogeneous mixing line of Beals *et al.* (2015). Furthermore, since the data cannot lie below the homogeneous mixing line of the global mixing process, a lower bound for $\mathscr{R}$ is $\mathscr{R}_{min} = \frac{2}{3}(n_* - r_*^3)n_* / \left[(1+s_c)(\chi_0 + n_*) - 1\right] = 0.0236$.

Figure 5b shows values of $\mathscr{R}$ and Da_d obtained from our statistical-model simulations that are consistent with these constraints. We see that the range of possible values of Da_d covers several orders of magnitude. This means that local mixing processes consistent with the red cross in Figure 5a may have occurred over a large range of spatial scales. We also see that $\mathscr{R}$ does not vary much in Figure 5b, only between 0.024 and 0.03. This allows us to conclude that some important aspects of the mixing dynamics are essentially independent of spatial scale. First, the fact that $\mathscr{R}$ is substantially smaller than 0.17 indicates that the non-cloudy air was premixed. Second, using Equation 11, we find that the reduction in droplet number density was caused primarily by dilution even at the largest scales, since P_e^* increases only up ~1.4% for the largest value of Da_d, at $Da_d \sim 1000$ and $\mathscr{R} = 0.03$. Put differently, $\chi \sim n_*$ for all values of Da_d we considered.

How does the outcome of a local mixing process depend on its scale? Larger scales correspond to larger values of Da_d, and Figure 5b shows that complete droplet evaporation begins to occur around $Da_d = 1$, where $\mathscr{R}$ starts to exceed $\mathscr{R}_{min}$ (blue circle). Estimating $\varepsilon \sim 10$ cm^2·s^{-3}, a typical value for convective clouds (Devenish *et al.*, 2012), we find that $Da_d = 1$, $\tau_s \sim 1$, and $\mathscr{R} = \mathscr{R}_{min}$ correspond to the spatial scale 9 m. Mixing processes leading to the red cross in Figure 5a that occurred at scales smaller than 9 m were therefore perfectly homogeneous: none of the droplets evaporated completely, as they were diluted by premixed air. At larger spatial scales, small but nonzero fractions of the droplets evaporated completely. Equation 11 gives $\mathscr{R} = 0.028$ for $P_e^* = 1\%$, and from Figure 5b we read off $Da_d = 13$ (green circle). For $\varepsilon \sim 10$ cm^2 ·s^{-3} these values correspond to 300 m. This suggests that reductions in droplet number density are also

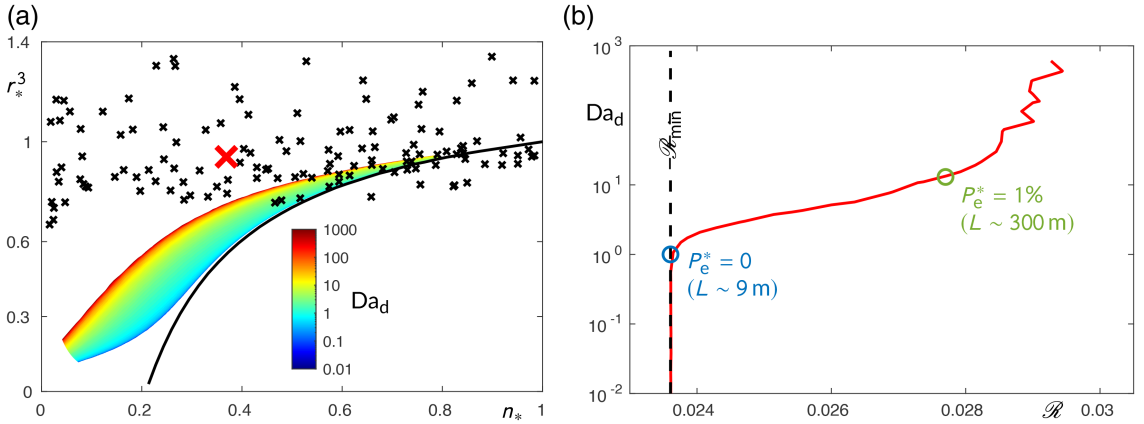

FIGURE 5 (a) Mixing diagram. Empirical data from Beals *et al.*, (2015) (black crosses). The homogeneous mixing line (black) from the top panel of figure 3 of Beals *et al.*, (2015) corresponds to $\mathscr{R} = 0.17$. The coloured region shows where steady states are found in the mixing diagram, for $\mathscr{R} = 0.17$. The corresponding values of $\mathrm{Da_d}$ are colour-coded (legend). The red cross is the measurement shown in the middle panel of figure 2 of Beals *et al.* (2015). (b) Values of $\mathscr{R}$ and $\mathrm{Da_d}$ consistent with a steady state at the red cross in panel (a) (red). We estimate $L \sim 9$ m for $\mathrm{Da_d} = 1$ (blue circle). These local mixing processes have $\mathscr{R} = \mathscr{R}_{\min}$ (black dashed line), so no droplets have evaporated completely ($P_e^* = 0$). The green circle corresponds to $\mathrm{Da_d} = 13$ and $\mathscr{R} = 0.028$, with $Pe^* = 1\%$ and $L \sim 300$ m.

TABLE 2 Parameters of DNS shown in Figure 4: Damköhler number $\mathrm{Da_d}$, Damköhler-number ratio $\mathscr{R}$, critical ratio $\mathscr{R}_c$, and volume fraction χ of cloudy air. Some dimensional parameters are also shown: domain size L, mean dissipation rate ε, and droplet number density n_0 of the initially cloudy air

	Nondimensional parameters					Dimensional parameters		
Reference	$\mathrm{Da_d}$	$\mathrm{Da_s}$	$\mathscr{R}$	$\mathscr{R}_c$	χ	L [cm]	ε [$\mathrm{cm^2\,s^{-3}}$]	n_0 [$\mathrm{cm^{-3}}$]
○ Andrejczuk *et al.* (2006)	$8E^{-1}$–$1E^{2}$	$3E^{0}$–$3E^{2}$	0.13–2.8	0.10–4.5	0.13–0.87	64	$4E^{-1}$–$9E^{2}$	$1E^{2}$–$1E^{3}$
△ Kumar *et al.* (2012)	$8E^{-3}$–$8E^{-1}$	$8E^{-2}$–$8E^{0}$	$9.2E^{-2}$	0.68	0.4	26	34	164
□ Kumar *et al.* (2013)	0.14, 0.31	0.62, 0.41	0.22, 0.73	0.68	0.4	26	34	164
◇ Kumar *et al.* (2014)	0.61–2.4	0.97–1.9	0.31–2.5	0.84	0.42	51	34	153
▽ Kumar *et al.* (2018)	0.12–0.91	0.51-4.0	0.23	0.90–0.95	0.42–0.45	$1E^{1}$–$2E^{2}$	32–35	120

dominated by dilution, and not complete droplet evaporation, for mixing processes that range over hundreds of metres. Furthermore, since most data points in Figure 5a reside well above the region where equilibria are found for $\mathscr{R} = 0.17$, we conclude that they too resulted from mixing with premixed air.

4 | DISCUSSION

A general conclusion from our analysis is that both Damköhler numbers are important for the transition to inhomogeneous mixing; $\mathrm{Da_d}$ parameterises the mixing-limited nature of droplet evaporation, and the ratio $\mathscr{R} = \mathrm{Da_d}/\mathrm{Da_s}$ regulates the self-limiting effect of droplet evaporation, namely that droplets cease to evaporate when they have saturated the surrounding air or evaporated completely. Analysing the parameters of our microscopic equations, Equations 1–4, we see that $\mathscr{R} = -\frac{3}{2}R$, where R is the potential evaporation parameter of Pinsky *et al.* (2016a) and Pinsky and Khain (2018a). Therefore R is in fact given by the ratio of $\mathrm{Da_d}$ and $\mathrm{Da_s}$, consistent with our conclusion that both Damköhler numbers matter.

Pinsky and Khain (2018b; 2019) concluded that the Damköhler-number ratio $\mathscr{R}$ determines whether a cloud expands by dilution or shrinks by complete droplet evaporation. A mixing process that mixes equal proportions of saturated cloudy and subsaturated noncloudy air has $\mathscr{R}_c = \frac{2}{3}$, so the symmetric configuration they adopted for the cloud edge implies that the cloud expands if $\mathscr{R} < \frac{2}{3}$ and shrinks otherwise. We note that whether the cloud expands or shrinks depends on the position and scale at which one perceives it. A local mixing process with small $\mathscr{R}/\mathscr{R}_c$ tends towards a moist steady state, so the cloud dilutes locally. A local mixing process that tends towards a dry steady state, by contrast, consumes the cloud. It

is possible for a cloud to expand locally for some time, even if this local expansion is part of a mixing process that consumes the cloud at larger length- and time-scales. Although global mixing processes are transient, they contain local steady states. Diluted and saturated local droplet populations (such as the red cross in Figure 5a) can be a part of such transients. However, such local steady states must eventually be abandoned as mixing proceeds globally.

Adopting this multiscale picture of mixing, in which a large-scale mixing process consists of many mixing processes at smaller scales, it is natural to expect that large ranges of the parameters χ, $\mathscr{R}$, and $\mathrm{Da_d}$ are relevant. If one moves the domain of a local mixing process from the interior of the cloud towards the cloud edge, the liquid water content decreases, so that $\mathscr{R}/\mathscr{R}_\mathrm{c}$ and $\mathrm{Da_d}$ increase. Lehmann *et al.* (2009) point out that $\mathrm{Da_d}$ increases as one perceives mixing processes at larger and larger spatial scales. This corresponds to moving to the right in Figure 4. We note that $\mathscr{R}/\mathscr{R}_\mathrm{c}$ and $\mathrm{Da_d}$ tend to increase with distance from the interior of the cloud. Moving the sampling volume towards the cloud edge then corresponds to a motion upwards and to the right in Figure 4. The amount of complete droplet evaporation increases in this direction, consistent with the fact that complete droplet evaporation takes place at the cloud edge.

A number of assumptions may influence our interpretation of the empirical data in Section 3.2. First, the model configuration in Figure 1b is simplified compared with real clouds, which have irregular shapes that deform during the mixing–evaporation process. Second, the observational method may not detect droplets with radii smaller than 3 μm ($r_\alpha^3 = 0.2$), as stated by Beals *et al.* (2015). If many small droplets were not detected, the observations in Figure 5a are located too far from the homogeneous mixing line. Third, at the upper end of the Damköhler range in Figure 5, the statistical model may not be quantitatively accurate, as stated above. We nevertheless expect that the statistical model reproduces the evolution of droplet size distributions in DNS qualitatively in Figure 5. This expectation is corroborated by the robust tendency for P_e^* to increase with increasing values of $\mathrm{Da_d}$ and $\mathscr{R}$ in Figure 4, and follows directly from the roles of the Damköhler numbers in mixing–evaporation dynamics.

The deviations in the tails of droplet size distributions at moderate Damköhler numbers in Figure 3 suggest that the next step in improving the statistical model should aim at reproducing the fastest evaporation rates in the transient mixing–evaporation process. A better agreement in the tails could be achieved by refining the closure for supersaturation diffusion by using a dynamic C_ϕ in Equation 7 (Jenny *et al.*, 2012), or by introducing additional fluctuations (Pope, 1991). Another possibility is to refine the description of the spatial structure of the supersaturation field by improved closures (Pope, 1991; Vedula *et al.*, 2001; Meyer and Jenny, 2008; Jenny *et al.*, 2012).

5 | CONCLUSIONS

We derived a statistical model for evaporation and turbulent mixing at the cloud edge from first principles. The model explains results of earlier DNS studies of mixing (Andrejczuk *et al.*, 2006; Kumar *et al.*, 2012; 2013; 2014; 2018) and shows that two thermodynamic time-scales are important for a mixing process, the droplet evaporation time and the supersaturation relaxation time. This means that one must consider two Damköhler numbers in order to quantify the mixing–evaporation dynamics. We concluded that the simulations of Kumar *et al.* (2018) did not exhibit a transition to inhomogeneous mixing with increasing spatial scale, because the supersaturation relaxation time was too small compared to the droplet evaporation time.

Our analysis supports general conclusions regarding in-situ observation of droplets in turbulent clouds. First, most of the local and instantaneous snapshots of droplet configurations observed by Beals *et al.* (2015) cannot be in the steady states of a global mixing process that mixed undiluted cloud with dry environmental air. However, a local droplet population may still be in a local steady state, established as the droplets saturated the air locally. Such local steady states belong to the transient of a global mixing process. In order to understand the nature of this transient, it was necessary to consider the whole range of possible steady states at different length-scales (Figure 1a). In short, clouds are not equilibrated at large scales, yet local steady states occur at small scales.

Our analysis also indicates that most of the droplet populations observed by Beals *et al.* (2015) are likely to have resulted from mixing with premixed air, and we concluded that the corresponding local steady states arose by dilution rather than complete evaporation. Our model indicates that only a very few droplets evaporated completely.

We found that the statistical-model dynamics is somewhat slower than the DNS of Kumar *et al.* (2012; 2014) and that the tails of our droplet size distributions are somewhat lighter. We speculated that this may be due to the supersaturation dynamics being oversimplified. Since our model belongs to the family of established PDF models (Pope, 2000), it is clear how to address this question in the future (Pope, 1991; Vedula *et al.*, 2001; Jenny *et al.*, 2012).

Last but not least, our analysis highlights which additional observational data are needed for a more quantitative statistical-model analysis of in situ cloud-droplet

measurements. To determine the three key parameters, the volume fraction of cloudy air as well as the two Damköhler numbers, one needs joint measurements of local droplet populations, supersaturation levels in their vicinity, and the sizes of the local cloud structures. This will allow us to characterise and understand the mechanisms underlying local mixing processes observed on different length- and time-scales and at different distances from the cloud edge. A challenge for the future is to understand the global picture, how evaporation distributes in the cloud, and where complete droplet evaporation takes place. This is necessary to improve the parameterisation of mixing and evaporation at the cloud edge in subgrid-scale models, in order to better represent the radiative effects of clouds.

ACKNOWLEDGEMENTS

J.F. and B.M. thank B. Kumar and J. Schumacher for providing details of their simulations. We acknowledge support from Vetenskapsrådet (grant number 2017-368 3865), Formas (grant number 2014-585), and the grant "Bottlenecks for particle growth in turbulent aerosols" from the Knut and Alice Wallenberg Foundation, Dnr. KAW 2014.0048. Simulations were performed on resources at Chalmers Centre for Computational Science and Engineering (C3SE), provided by the Swedish National Infrastructure for Computing (SNIC).

ORCID

G. Svensson https://orcid.org/0000-0001-9074-7623
B. Mehlig https://orcid.org/0000-0002-3672-6538

REFERENCES

Abade, G.C., Grabowski, W.W. and Pawlowska, H. (2018) Broadening of cloud droplet spectra through eddy hopping: turbulent entraining parcel simulations. *Journal of the Atmospheric Sciences*, 75, 3365–3379.

Andrejczuk, M., Grabowski, W.W., Malinowski, S.P. and Smolarkiewicz, P.K. (2006) Numerical simulation of cloud–clear air interfacial mixing: effects on cloud microphysics. *Journal of the Atmospheric Sciences*, 63, 3204–3225.

Baker, M.B., Corbin, R.G. and Latham, J. (1980) The influence of entrainment on the evolution of cloud droplet spectra: I. A model of inhomogeneous mixing. *Quarterly Journal of the Royal Meteorological Society*, 106, 581–598.

Beals, M.J., Fugal, J.P., Shaw, R.A., Lu, J., Spuler, S.M. and Stith, J.L. (2015) Holographic measurements of inhomogeneous cloud mixing at the centimeter scale. *Science*, 350, 87–90.

Blyth, A.M. (1993) Entrainment in cumulus clouds. *Journal of Applied Meteorology*, 32, 626–641.

Bodenschatz, E., Malinowski, S.P., Shaw, R.A. and Stratmann, F. (2010) Can we understand clouds without turbulence? *Science*, 327, 970–971.

Burnet, F. and Brenguier, J.-L. (2007) Observational study of the entrainment–mixing process in warm convective clouds. *Journal of the Atmospheric Sciences*, 64, 1995–2011.

Caldwell, P.M., Zelinka, M.D., Taylor, K.E. and Marvel, K. (2016) Quantifying the sources of intermodel spread in equilibrium climate sensitivity. *Journal of Climate*, 29, 513–524.

Chandrakar, K.K., Cantrell, W., Chang, K., Ciochetto, D., Niedermeier, D., Ovchinnikov, M., Shaw, R.A. and Yang, F. (2016) Aerosol indirect effect from turbulence-induced broadening of cloud-droplet size distributions. *Proceedings of the National Academy of Sciences*, 113, 14243–14248.

Devenish, B.J., Bartello, P., Brenguier, J.-L., Collins, L.R., Grabowski, W.W., IJzermans, R.H.A., Malinowski, S.P., Reeks, M.W., Vassilicos, J.C., Wang, L.-P. and Warhaft, Z. (2012) Droplet growth in warm turbulent clouds. *Quarterly Journal of the Royal Meteorological Society*, 138, 1401–1429.

Dimotakis, P.E. (2005) Turbulent mixing. *Annual Review of Fluid Mechanics*, 37, 329–356.

Dufresne, J.-L. and Bony, S. (2008) An assessment of the primary sources of spread of global warming estimates from coupled atmosphere–ocean models. *Journal of Climate*, 21, 5135–5144.

Eswaran, V. and Pope, S. (1988) Direct numerical simulations of the turbulent mixing of a passive scalar. *Physics of Fluids*, 31, 506–520.

Frisch, U. (1995) *Turbulence: The Legacy of A. N. Kolmogorov*. Cambridge, UK: Cambridge University Press.

Gerber, H.E., Frick, G.M., Jensen, J.B. and Hudson, J.G. (2008) Entrainment, mixing, and microphysics in trade-wind cumulus. *Journal of the Meteorological Society of Japan*, 86A, 87–106.

Grabowski, W.W. and Wang, L.-P. (2013) Growth of cloud droplets in a turbulent environment. *Annual Review of Fluid Mechanics*, 45, 293–324.

Gustavsson, K. and Mehlig, B. (2016) Statistical models for spatial patterns of heavy particles in turbulence. *Advances in Physics*, 65, 1–57.

Haworth, D.C. (2010) Progress in probability density function methods for turbulent reacting flows. *Progress in Energy and Combustion Science*, 36, 168–259.

Hoffmann, F. and Feingold, G. (2019) Entrainment and mixing in stratocumulus: effects of a new explicit subgrid-scale scheme for large-eddy simulations with particle-based microphysics. *Journal of the Atmospheric Sciences*, 76, 1955–1973.

Jeffery, C.A. (2007) Inhomogeneous cloud evaporation, invariance, and Damköhler number. *Journal of Geophysical Research*, 112, D24S21.

Jenny, P., Roekaerts, D. and Beishuizen, N. (2012) Modeling of turbulent dilute spray combustion. *Progress in Energy and Combustion Science*, 38, 846–887.

Kokhanovsky, A. (2004) Optical properties of terrestrial clouds. *Earth-Science Reviews*, 64, 189–241.

Kumar, B., Götzfried, P., Suresh, N., Schumacher, J. and Shaw, R.A. (2018) Scale dependence of cloud microphysical response to turbulent entrainment and mixing. *Journal of Advances in Modeling Earth Systems*, 10, 2777–2785.

Kumar, B., Janetzko, F., Schumacher, J. and Shaw, R.A. (2012) Extreme responses of a coupled scalar–particle system during turbulent mixing. *New Journal of Physics*, 14, 115020.

Kumar, B., Schumacher, J. and Shaw, R.A. (2013) Cloud microphysical effects of turbulent mixing and entrainment. *Theoretical and Computational Fluid Dynamics*, 27, 361–376.

Kumar, B., Schumacher, J. and Shaw, R.A. (2014) Lagrangian mixing dynamics at the cloudy–clear air interface. *Journal of the Atmospheric Sciences*, 71, 2564–2580.

Lamb, D. and Verlinde, J. (2011) *Physics and Chemistry of Clouds*. Cambridge, UK: Cambridge University Press.

Lanotte, A.S., Seminara, A. and Toschi, F. (2009) Cloud droplet growth by condensation in homogeneous isotropic turbulence. *Journal of the Atmospheric Sciences*, 66, 1685–1697.

Lehmann, K., Siebert, H. and Shaw, R.A. (2009) Homogeneous and inhomogeneous mixing in cumulus clouds: dependence on local turbulence structure. *Journal of the Atmospheric Sciences*, 66, 3641–3659.

Li, X.-Y., Brandenburg, A., Svensson, G., Haugen, N.E.L., Mehlig, B. and Rogachevskii, I. (2020) Condensational and collisional growth of cloud droplets in a turbulent environment. *Journal of the Atmospheric Sciences*, 77, 337–353.

Lu, C., Liu, Y., Zhu, B., Yum, S.S., Krueger, S.K., Qiu, Y., Niu, S. and Luo, S. (2018) On which microphysical time-scales to use in studies of entrainment–mixing mechanisms in clouds. *Journal of Geophysical Research: Atmospheres*, 123, 3740–3756.

Mauritsen, T., Stevens, B., Roeckner, E., Crueger, T., Esch, M., Giorgetta, M., Haak, H., Jungclaus, J., Klocke, D., Matei, D., Mikolajewicz, U., Notz, D., Pincus, R., Schmidt, H. and Tomassini, L. (2012) Tuning the climate of a global model. *Journal of Advances in Modeling Earth Systems*, 4, 1–18.

Meyer, D.W. and Jenny, P. (2008) An improved mixing model providing joint statistics of scalar and scalar dissipation. *Combustion and Flame*, 155, 490–508.

Paoli, R. and Shariff, K. (2009) Turbulent condensation of droplets: direct simulation and a stochastic model. *Journal of the Atmospheric Sciences*, 66, 723–740.

Perrin, V.E. and Jonker, H.J.J. (2015) Lagrangian droplet dynamics in the subsiding shell of a cloud using direct numerical simulations. *Journal of the Atmospheric Sciences*, 72, 4015–4028.

Pincus, R., Winker, D., Bony, S. and Stevens, B. (2018) *Shallow Clouds, Water Vapor, Circulation, and Climate Sensitivity*. Cham, Switzerland: Springer International Publishing AG.

Pinsky, M. and Khain, A. (2018a) Theoretical analysis of mixing in liquid clouds – Part 4: DSD evolution and mixing diagrams. *Atmospheric Chemistry and Physics*, 18, 3659–3676.

Pinsky, M. and Khain, A. (2018b) Theoretical analysis of the entrainment–mixing process at cloud boundaries. Part I: droplet size distributions and humidity within the interface zone. *Journal of the Atmospheric Sciences*, 75, 2049–2064.

Pinsky, M. and Khain, A. (2019) Theoretical analysis of the entrainment–mixing process at cloud boundaries. Part II: motion of cloud interface. *Journal of the Atmospheric Sciences*, 76, 2599–2616.

Pinsky, M., Khain, A. and Korolev, A. (2016a) Theoretical analysis of mixing in liquid clouds – Part 3: inhomogeneous mixing. *Atmospheric Chemistry and Physics*, 16, 9273–9297.

Pinsky, M., Khain, A., Korolev, A. and Magaritz-Ronen, L. (2016b) Theoretical investigation of mixing in warm clouds – Part 2: homogeneous mixing. *Atmospheric Chemistry and Physics*, 16, 9255–9272.

Pope, S. (1991) Mapping closures for turbulent mixing and reaction. *Theoretical and Computational Fluid Dynamics*, 2, 255–270.

Pope, S.B. (1985) PDF methods for turbulent reactive flows. *Progress in Energy and Combustion Science*, 11, 119–192.

Pope, S.B. (2000) *Turbulent Flows*. Cambridge, UK: Cambridge University Press.

Pope, S.B. (2011) Simple models of turbulent flows. *Physics of Fluids*, 23, 1–20.

Pope, S.B. and Chen, Y.L. (1990) The velocity-dissipation probability density function model for turbulent flows. *Physics of Fluids*, 2, 1437–1449.

Rogers, R.R. and Yau, M.K. (1989) *A Short Course in Cloud Physics*. Oxford: Pergamon Press.

Sardina, G., Picano, F., Brandt, L. and Caballero, R. (2015) Continuous growth of droplet size variance due to condensation in turbulent clouds. *Physical Review Letters*, 115, 184501.

Sardina, G., Poulain, S., Brandt, L. and Caballero, R. (2018) Broadening of cloud droplet size spectra by stochastic condensation: effects of mean updraft velocity and CCN activation. *Journal of the Atmospheric Sciences*, 75, 451–467.

Shraiman, B.I. and Siggia, E.D. (2000) Scalar turbulence. *Nature*, 405, 639–646.

Siewert, C., Bec, J. and Krstulovic, G. (2017) Statistical steady state in turbulent droplet condensation. *Journal of Fluid Mechanics*, 810, 254–280.

Stocker, T., Qin, D., Plattner, G.-K., Tignor, M., Allen, S., Boschung, J., Nauels, A., Xia, Y., Bex, V. and Midgley, P. (Eds.) (2013) *Climate Change 2013: The Physical Science Basis. Contribution of Working Group I to the Fifth Assessment Report of the Intergovernmental Panel on Climate Change*. Cambridge, UK: Cambridge University Press.

Stöllinger, M., Naud, B., Roekaerts, D., Beishuizen, N. and Heinz, S. (2013) PDF modeling and simulations of pulverized coal combustion–Part 1: theory and modeling. *Combustion and Flame*, 160, 384–395.

Szumowski, M.J., Rauber, R.M., Ochs, H.T. and Beard, K.V. (1998) The microphysical structure and evolution of Hawaiian rainband clouds. Part II: aircraft measurements within rainbands containing high reflectivity cores. *Journal of the Atmospheric Sciences*, 55, 208–226.

Szumowski, M.J., Rauber, R.M., Ochs, H.T. and Miller, L. (1997) The microphysical structure and evolution of Hawaiian rainband clouds. Part I: radar observations of rainbands containing high reflectivity cores. *Journal of the Atmospheric Sciences*, 54, 369–385.

Tölle, M.H. and Krueger, S.K. (2014) Effects of entrainment and mixing on droplet size distributions in warm cumulus clouds. *Journal of Advances in Modeling Earth Systems*, 6, 281–299.

Vaillancourt, P.A., Yau, M.K., Bartello, P. and Grabowski, W.W. (2002) Microscopic approach to cloud droplet growth by condensation. Part II: turbulence, clustering, and condensational growth. *Journal of the Atmospheric Sciences*, 59, 3421–3435.

Vaillancourt, P.A., Yau, M.K. and Grabowski, W.W. (2001) Microscopic approach to cloud droplet growth by condensation. Part I: model description and results without turbulence. *Journal of the Atmospheric Sciences*, 58, 1945–1964.

Vedula, P., Yeung, P. and Fox, R.O. (2001) Dynamics of scalar dissipation in isotropic turbulence: a numerical and modelling study. *Journal of Fluid Mechanics*, 433, 29.

SUPPORTING INFORMATION

Additional supporting information may be found online in the Supporting Information section at the end of this article.

How to cite this article: Fries J, Sardina G, Svensson G, Mehlig B. Key parameters for droplet evaporation and mixing at the cloud edge. *QJR Meteorol. Soc*. 2021;1–13. https://doi.org/10.1002/qj.4015

APPENDIX A. LIST OF SYMBOLS

Table A1 lists symbols used in the article.

TABLE A1 List of symbols

t	time
$\boldsymbol{x} = (x, y, z)$	spatial position
N_0	number of droplets at initialisation
P_e	fraction of completely evaporated droplets
$\boldsymbol{u}$	fluid velocity
p	pressure
L	side length of cubic simulation domain
w	width of initially cloudy region in simulation domain
s_c	supersaturation within initial cloud slab
s_e	supersaturation outside initial cloud slab
TKE	turbulent kinetic energy
U	root-mean-square of fluid velocity
ε	turbulent dissipation rate per unit mass
ν	kinematic viscosity
κ	diffusivity of supersaturation
s	supersaturation
r	droplet radius
r_0	initial volume radius of droplets
n_0	droplet number density of intially cloudy region
$\overline{r_\alpha(t)s(\boldsymbol{x}_\alpha, t)}$	average of $r_\alpha(t)s(\boldsymbol{x}_\alpha, t)$ for droplets in the vicinity of $\boldsymbol{x}$ at time t
$\frac{D}{Dt}$	Lagrangian time derivative
τ_d	droplet evaporation time
τ_s	supersaturation relaxation time
τ_ℓ	time-scale for mixing at the length scale ℓ
τ_L	large-eddy turnover time in simulation domain
Re_L	turbulence Reynolds number
Sc	Schmidt number
V	nondimensional volume of simulation domain
Da_d	Damköhler number based on droplet evaporation time
Da_s	Damköhler number based on supersaturation relaxation time
$\mathscr{R}$	Damköhler-number ratio
$\mathscr{R}_\mathrm{c}$	Critical Damköhler-number ratio
$\mathscr{R}_\mathrm{min}$	Lower bound for Damköhler-number ratio related to mixing diagrams
χ	volume fraction of cloudy air
χ_0	contribution to the initial volume average of supersaturation
θ	conserved quantity that reflects the conservation of water and energy
C_0, C_ϕ	empirical constants
$\langle \dots \rangle$	volume average or ensemble average in statistical model